

Observation of Reconstructable Radio Emission Coincident with an X-Class Solar Flare in the Askaryan Radio Array Prototype Station

P. Allison^a, S. Archambault^b, J. Auffenberg^c, R. Bard^d, J. J. Beatty^{a,e}, M. Beheler-Amass^c, D. Z. Besson^{f,g}, M. Beydler^c, C. Bora^h, C.-C. Chenⁱ, C.-H. Chenⁱ, P. Chenⁱ, B. A. Clark^{a,*}, A. Clough^h, A. Connolly^{a,*}, L. Cremonesi^j, J. Davies^j, C. Deaconu^k, M. A. DuVernois^c, E. Friedman^d, B. Fox^l, P. W. Gorham^l, J. Hanson^m, K. Hanson^c, J. Haugen^c, B. Hill^l, K. D. Hoffman^d, E. Hong^{a,*}, S.-Y. Hsuⁱ, L. Huiⁱ, J.-J. Huangⁱ, M.-H. Huangⁱ, A. Ishihara^b, A. Karle^c, J. L. Kelley^c, R. Khandelwal^c, M. Kim^b, I. Kravchenko^h, J. Kruse^h, K. Kurusu^b, H. Landsmanⁿ, U. A. Latif^f, A. Laundrie^c, C.-J. Liⁱ, T. C. Liuⁱ, M.-Y. Lu^c, K. Mase^b, R. Maunu^d, T. Meures^c, C. Miki^l, J. Namⁱ, R. J. Nichol^j, G. Nirⁿ, E. Oberla^k, A. ÓMurchadha^c, Y. Pan^o, C. Pfendner^{a,*}, K. Ratzlaff^f, M. Richman^d, J. Roth^o, B. Rotter^l, P. Sandstrom^c, D. Seckel^o, Y.-S. Shiaoⁱ, A. Shultz^h, M. Song^d, J. Stockham^f, M. Stockham^f, M. Sullivan^p, J. Touart^d, H.-Y. Tuⁱ, G. S. Varner^l, A. G. Vieregg^k, M.-Z. Wangⁱ, S.-H. Wangⁱ, S. A. Wissel^q, S. Yoshida^b, R. Young^f

^aDept. of Physics and Center for Cosmology and AstroParticle Physics, The Ohio State University, Columbus, OH, USA

^bDept. of Physics, Chiba University, Tokyo, Japan

^cDept. of Physics and Wisconsin IceCube Particle Astrophysics Center, University of Wisconsin, Madison, WI, USA

^dDept. of Physics, University of Maryland, College Park, MD, USA

^eDept. of Astronomy, The Ohio State University, Columbus, OH USA

^fDept. of Physics and Astronomy and Instrumentation Design Laboratory, University of Kansas, Lawrence, KS, USA

^gNational Research Nuclear University, Moscow Engineering Physics Institute, Moscow, Russia

^hDept. of Physics and Astronomy, University of Nebraska-Lincoln, Lincoln, NE, USA

ⁱDept. of Physics, Grad. Inst. of Astrophys., Leung Center for Cosmology and Particle Astrophys., National Taiwan Univ., Taipei, Taiwan

^jDept. of Physics and Astronomy, University College London, London, UK

^kDept. of Physics and Kavli Institute for Cosmological Physics, The University of Chicago, Chicago, IL, USA

^lDept. of Physics and Astronomy, University of Hawaii-Manoa, Honolulu, HI, USA

^mDept. of Physics and Astronomy, Whittier College, Whittier, CA, USA

ⁿWeizmann Institute of Science, Rehovot, Israel

^oDept. of Physics and Astronomy, University of Delaware, Newark, DE, USA

^pMoscow Engineering and Physics Institute, Moscow, Russia

^qDept. of Physics, California Polytechnic State University, San Luis Obispo, CA, USA

Abstract

The Askaryan Radio Array (ARA) reports an observation of radio emission coincident with the “Valentine’s Day” solar flare on Feb. 15th, 2011 in the prototype “Testbed” station. We find ~ 2000 events that passed our neutrino search criteria during the 70 minute period of the flare, all of which reconstruct to the location of the sun. A signal analysis of the events reveals them to be consistent with that of bright thermal noise correlated across antennas. This is the first natural source of radio emission reported by ARA that is tightly reconstructable on an event-by-event basis. The observation is also the first for ARA to point radio from individual events to an extraterrestrial source on the sky. We comment on how the solar flares, coupled with improved systematic uncertainties in reconstruction algorithms, could aid in a mapping of any above-ice radio emission, such as that from cosmic-ray air showers, to astronomical locations on the sky.

Keywords: solar flare, radio neutrino telescope

1. Introduction

The Askaryan Radio Array (ARA) is a radio array designed to detect ultra-high energy (UHE) neutrinos via their radio-Cherenkov emission in ice [1, 2]. The array consists of 150-850 MHz antennas buried in the ice at 200 m

depth. The signature of a UHE neutrino would be an impulsive signal that originates from a neutrino-induced cascade of charged particles in the otherwise quiet ice.

The ARA Collaboration plans to deploy a 100-km² array at 200 m depth in the ice near the South Pole. So far, five deep stations have been deployed—one in 2012, two in 2013, and another two in 2018. In 2011, prior to the deep deployments, an initial prototype “Testbed” station was deployed at ~ 30 m depth to assess the level of anthropogenic and natural backgrounds at radio frequencies, clarity of ice near the South Pole in our frequency band,

*Corresponding Authors

Email addresses: clark.2668@osu.edu (B. A. Clark), connolly@physics.osu.edu (A. Connolly), ripple80@gmail.com (E. Hong), pfendner.1@osu.edu (C. Pfendner)

and to test potential designs.

We report on an observation of radio emission from the sun that is coincident in time with the Feb. 15th, 2011 “Valentine’s Day” solar flare. The radio emission arrives with relative time delays among our antennas that indicate a direction to its origin that tracks the sun’s movement—with a 2° degree systematic offset in azimuth, and 10° systematic offset in elevation—over the 70 minute duration of the flare. The radiation was generated at the sun and propagated to earth, and is not the neutrino-associated Askaryan radiation the array was designed to detect.

The events are the first reported by ARA to reconstruct radio on an event-by-event basis to an extraterrestrial source on the sky. As systematic uncertainties in reconstruction algorithms – such as errors in antenna positions and modeling of the depth-dependent index of refraction – are reduced, such events from a moving high-statistics, above ice emitter can be used to improve ARA’s mapping of above-ice RF sources to locations on the sky. This will be especially applicable to studies of the direction of cosmic rays which produce geomagnetic radio emission through extensive air showers.

The solar flare events reported here are different from solar-related emission previously reported by ARA from two days earlier on Feb. 13th [3] in that they have tight reconstructions and track the sun for an extended period of time; a more extensive discussion of the Feb. 13th flare can be found in Appendix D.

These events also aid ARA’s understanding of the radio sky. Sources of radio emission, both natural and human-made, can interfere with both triggering and data analysis. We would also like to be open to observations of astrophysical radio sources given ARA’s unusually large field of view with a broad bandwidth. To this end, we are able to build spectrograms that demonstrate the observation of type-II and type-IV solar radio emission that agrees with other radio observatories.

The paper is organized as follows. In Sec. 2, we describe the ARA Testbed instrument. In Sec. 3, we outline the main features of the radio emission observed from the flare, in terms of spectra and reconstructions. In Sec. 4, we present a signal analysis of the events demonstrating evidence for the hypothesis that they are correlated thermal noise from a point source. In Sec. 5, we discuss the potential of this and future solar flare detections in ARA, namely their potential role in understanding ARA’s response to above-ice RF sources like cosmic-ray air showers. In Sec. 6, we discuss a search for other solar flares with the Testbed and with deep ARA stations. In Sec. 7, we summarize our results.

2. The ARA Testbed Instrument

The Askaryan Radio Array (ARA) “Testbed” instrument is an array of 14 “high”-frequency (150-850 MHz) broadband antennas buried up to 30 m deep, and two

“low”-frequency (30-300 MHz) antennas placed at the surface. All are located at the South Pole with the goal of detecting ultra-high energy neutrinos via their radio-Cherenkov emission in ice. The Testbed was a prototype instrument deployed in January 2011 and operated until January 2013. The station’s main purpose was to assess the radio noise environment, measure ice properites, and explore design choices later utilized in a mature station; a full instrument description of the Testbed is available in [3]. Of the 14 higher-band antennas, the analysis presented in this paper primarily uses data from eight which were buried at a depth of ~30 m in “boreholes”: four vertically polarized (VPol) bicone antennas and four horizontally polarized (HPol) bowtie-slotted cylinder antennas. These antennas were selected for the analysis because, (a) for each polarization, the antennas have the same basic dipole-like design (bicone for VPol antennas, bowtie-slotted cylinder for HPol antennas), and (b) they have the same sampling rate of 2 GHz.

The station consists of two primary elements; “down-hole” components which receive and transmit the signal, and “surface” components which provide data acquisition and system control. Downhole components include the antennas, signal conditioning, and transmission to the surface. Surface components include additional signal conditioning, and triggering and digitization electronics.

The RF signal chain provides amplification and filtering in preparation for digitization and triggering. In the ice, the signal undergoes ~ 40 dB of low-noise amplification, a 450 MHz notch filter to remove South Pole communications signals, and is transmitted to surface electronics via radio-over-fiber (RFoF). At the surface, a transceiver returns it to electronic RF, and the signal undergoes an additional 40 dB of second stage amplification, a 150-850 MHz band-pass filter to remove out-of-band amplifier noise, and a splitting to trigger and digitizing paths.

In ARA, the trigger is designed to identify transient impulsive events and the digitizer records these signals with high fidelity. The trigger path routes to a tunnel diode, which functions as a ~ 5 ns power integrator. Any signal exceeding 5-6 times the mean thermal noise power in 3 out of 8 borehole antennas within a 110 ns time window triggers the digitization of all 16 antennas in the array. Signal to be digitized is sampled at 2 (1) GHz for borehole (shallow) antennas with a 12-bit custom digitizer. The digitization window is 250 ns wide, centered to within 10 ns on the trigger time. Impulsive events, which produce large integrated power over short time windows, naturally satisfy this trigger. The trigger will also fire if the blackbody thermal noise background of the ice randomly fluctuates high in a sufficient number of channels, or if some radio loud source illuminates the array.

3. Characteristics of Observed Radio Emission

The ARA team first noticed the events of interest in March 2014 during the final stages of a data analysis aimed

at searching for UHE neutrinos in the ARA prototype Testbed station [4]. In that analysis, we searched for events that did not have strong continuous-wave (CW) contamination, and that originated in the ice below the Testbed station. Their location of origin was determined through a peak in the cross-correlation of waveforms from different antennas across the station, accounting for delays in any hypothesized direction of origin.

The events of interest were discovered during final tests performed in the neutrino search, and were determined to originate from the Feb. 15th flare due to time coincidence and directional reconstruction that tracked the sun's location. By removing the original search requirement that the event's origin be in the ice below the station, we found 244 events were recorded in the time period from 02:04-02:58 Feb. 15th 2011 UTC in only 10% of the dataset used until "unblinding" the final stage of analysis. When the full 100% unblinded data set is examined, 2323 events between 02:01-02:58 UTC pass cuts. This time period was found to be coincident with the February 15th, 2011 X-2.2 solar flare, which the RHESSI Flare Survey webpage [5] reports to have begun at 01:43:44 UTC the same day in X-ray measurements. These events on Feb. 15th follow closely events from an M-class flare on Feb. 13th, which were reported on in the prototype instrument paper and are discussed further in Appendix D.

3.1. Trigger Rates and Spectra

Figure 1 shows that during the hour over which these 244 events were observed in 10% of the data, our trigger rates rose from a few Hz during a normal period to as much as 25 Hz. This maximum trigger rate is set by the deadtime during readout whenever a trigger is fired.

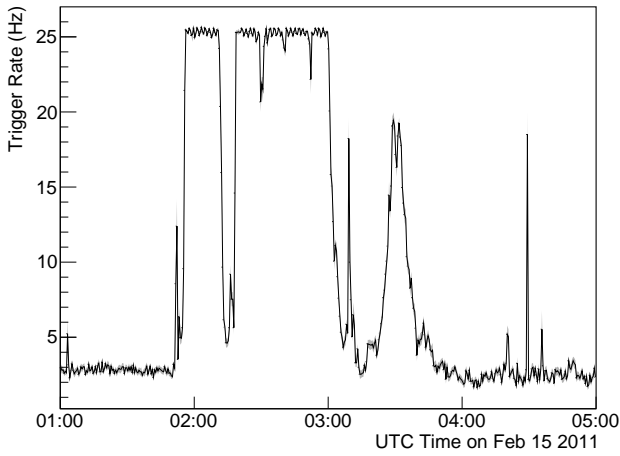


Figure 1: The Testbed global trigger rate during the solar flare. Before and after the flare, the instrument triggers near the predetermined "thermal-noise riding" rate [3]. The black line is the mean trigger rate per thirty second time bin, and the grey band is the standard error on that mean (that is, the square root of the number of entries per bin).

In Fig. 2, we show average spectra from one antenna (VPol) for the 2323 events observed in 100% of the data, compared with an average spectra over 2300 events from the forced trigger sample on Feb 11, dominated by thermal noise. One can see that over the period of the flare, the excess emission is predominantly in the 200-400 MHz portion of the band.

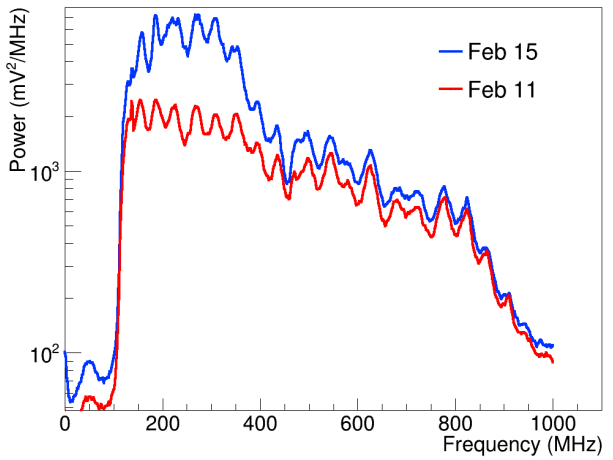


Figure 2: Average spectra of Channel 2 (VPol) for the 2323 events that pass analysis cuts designed for the neutrino search on Feb 15th (blue) and 2300 events between 2 AM and 3:00 AM that are thermal noise forced triggers (red) from Feb 11th. This shows the power excess observed between 200-400 MHz during this particular time of the flare. The small scale oscillations, present in both the flare and thermal noise sample, are attributed to instrumental characteristics. The lines are the mean of the distribution of spectral amplitudes in a given frequency bin; the distribution is an exponential, as is expected for the power spectrum of thermal noise plotted in the units of mV^2/MHz .

We create a spectrogram for the 01:30-03:00 UTC period and compare with those made by solar radio astronomers e.g. [6, 7]. In Fig. 3, we plot a background-subtracted spectrogram of a borehole VPol channel over the entire hour of the flare. The background spectrogram is constructed from an identical time window on February 11th, 2011, when the sun would have been in approximately the same position, but was not active.

The radio emission begins to saturate our trigger at approximately 01:57 UTC, roughly coinciding with the peak of the soft x-ray flux. Such coincidence is a feature typical of type-II flare radiation [6]. Two reference measurements of the peak soft x-ray flux are given by the RHESSI instrument (3-10 keV), which reports peaking at 01:55 UTC [5] and by the Fermi GBM (>10 keV coinciding with GOES observations), which reports peaking at 01:59 UTC [8].

The spectrograms, and their associated features between 150 and 500 MHz, agree with other radio observatories that classify this flare emission as type-II followed by type-IV. The Culgoora telescope, with sensitivity from 18-1800 MHz, records spectrograms comparable to our own and lists this flare in their type-II catalog [9].

3.2. Directional Reconstruction

The most striking feature of these events is how well they “reconstruct” uniquely to the sun, tracking the motion of the sun in azimuth during that hour. In other words, considering all hypothesized directions across the sky, we found the highest cross-correlation values in a direction within 2° in azimuth of the sun, without distinctly different directions also giving competitive cross-correlations for the same event. The azimuthal angle of the reconstruction peak has a 2° systematic offset from the true value of the sun’s azimuth. The events also track the solar position in elevation, but with a significant systematic offset, appearing $\sim 10^\circ$ higher in the sky than the true solar elevation. In this section, first we will review the method that we use to calculate cross-correlation values associated with positions on the sky before showing cross-correlation maps for a typical flare event. We also describe our calculations of coherently summed waveforms that we use to investigate the nature of the correlated noise component of these events.

3.2.1. Reconstruction in ARA Analyses

In order to determine the direction of the source of radio signals, we use an interferometric technique similar to the one used in a search for a flux of diffuse neutrinos using data from the ARA Testbed station that takes into account the index of refraction of the ice surrounding the antennas [4]. We first map the cross-correlation function from pairs of waveforms from two different antennas to expected arrival delays from different putative source directions. For each direction on the sky, the mapped cross-correlations from many pairs of antennas are added together and where the delays between different pairs of antennas signals have the strongest agreement, there is a peak in the correlation map.

For a given pair of antenna waveforms, the cross-correlation between the voltage waveform on the i -th antenna ($f_i(t)$) and the voltage waveform on the j -th antenna ($(g_j(t))$ as a function of time lag τ can be found from Eq. 1:

$$C_{i,j}(\tau) = \sum_{t=-\infty}^{\infty} f_i(t)g_j(t+\tau) \quad (1)$$

The time lag τ depends on the position of the source relative to the array, characterized as elevation angle θ , azimuthal angle ϕ , and the distance R to the source; the origin of this coordinate system is defined as the average of the positions of the antennas contributing to the map. As in [4], we only consider two hypothesized distances, 30 m and 3000 m. In the original diffuse analysis, these were chosen because 30 m is roughly the distance of the local calibration pulser, and 3000 m is an estimate for a far-field emitter like a neutrino interaction. The total cross-correlation strength for a given point on the sky (θ, ϕ) is given by summing over all like polarization pairs

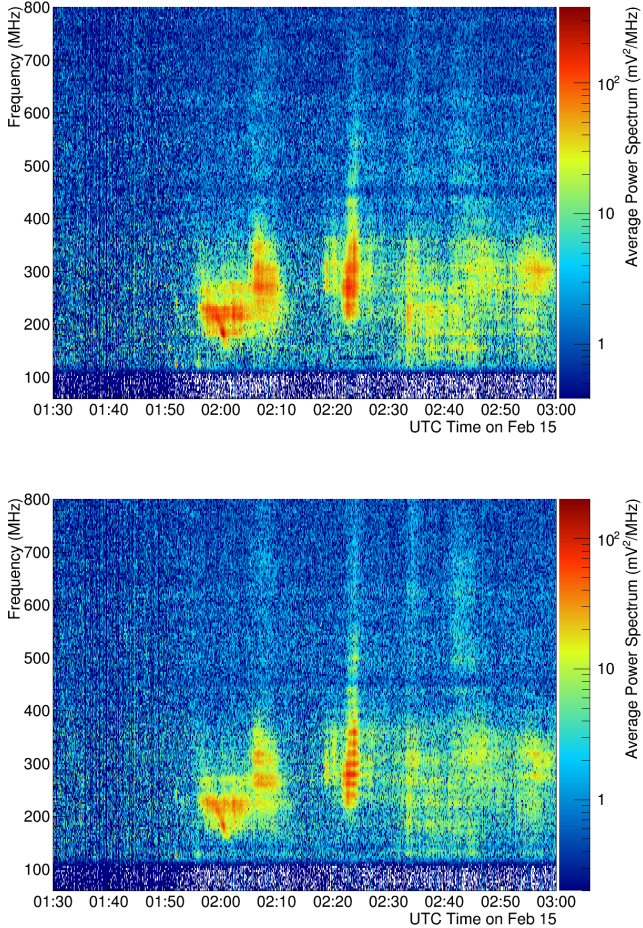


Figure 3: (Top) A background-subtracted spectrogram of Channel 2 of the Testbed, for the hour from the beginning of the flare. The background sample is taken from an identical time period on Feb. 11th (four days prior) when the sun was not flaring. (Bottom) A background-subtracted spectrogram produced from the coherently-summed waveform from two channels (Channels 3 and 4) given the delay relative to one another that gives the strongest cross-correlation value. Note that the coherently-summed spectrogram demonstrates that many features are shared between antennas. We only use two channels, as opposed to four channels combined with a directional hypothesis, to avoid a reduction in the signal strength due to any timing misalignments for a given directional hypothesis.

of antennas as in Eq. 2

$$C(\theta, \phi; R) = \sum_{i=1}^{n_{ant}-1} \sum_{j=i+1}^{n_{ant}} C_{i,j}[\tau(\theta, \phi; R)] \quad (2)$$

Plotting this total cross-correlation strength for all points on the sky yields a correlation map, as is shown in Fig. 4. The azimuth and elevation correspond to the position on the sky of a putative emitter relative to the station center.

The arrival delays τ are found by calculating a path from a hypothesized source location to an antenna through an ice model that accounts for the changing index of the Antarctic firn. We consider a constant $n = 1$ index of refraction in the air. The ray-tracing method models the changing index of refraction as follows:

$$n(z) = 1.78 - 1.35e^{0.0132z} \quad (3)$$

This index of refraction model is taken from a fit to data taken by the RICE experiment [10], and is the same as the one used in [4]. To smooth uncertainties in this ice model and other systematics, we calculate the Hilbert envelope of the cross-correlation function before summing over pairs, as is done in previous analyses [4, 11].

3.2.2. Reconstructed Directions Track the Sun

Figs. 4 shows maps of cross-correlation values obtained by considering directions across the sky for the same event as shown in Figs. 8 in the Appendix. Comparison plots from a quiescent period can be found in Appendix A. Note that we find the strongest cross-correlation values when we consider the $R = 30$ m hypothesis rather than the $R = 3000$ m hypothesis. Although, the peak in the cross-correlation map has an elevation that is closer to the true elevation of the sun in the $R = 3000$ m case.

We attribute the offsets in the azimuth and elevation of the reconstruction peak, as well as the higher correlation peak value at the near radius, to coupled systematics uncertainties associated with our reconstruction algorithms. This includes the orientation of the local surface normal \hat{n} , the parameterization of the depth-dependent index of refraction $n(z)$, variations of the index-of-refraction at the surface due to blowing snow and human activity, unknown cable delays at the level of 1-2 ns, and surveying uncertainties at the level of 10-20 cm. The relative importance of these various systematics is under ongoing study.

The top panel of Fig. 5 show the reconstructed directions for all events passing cuts as a function of time for the duration of the flare, taken from the peak of the maps for the $R = 3000$ m hypothesis. The events during this time period reconstructed to a direction within a few degrees in azimuth and approximately 10° in elevation angle of the sun's position in the sky, appearing higher than the known location of the sun (13.3°). We note that the second increase in trigger rates in Fig. 1 around 03:30 UTC does include a set of ~ 200 events that also reconstruct to the sun, but do not pass any analysis cuts. We do not

study them in depth, and instead focus on the emission from 01:50-03:00 UTC where many events pass analysis cuts and we have direct overlap with results from other solar observatories.

3.3. Coherently Summed Waveforms

In addition to building a correlation map, we can construct coherently summed waveforms (CSWs) from antennas of like polarization by first delaying the waveforms with respect to each other by a τ that is specific to an antenna pair, and then summing. For a set of τ 's corresponding to the direction of the source, the CSW should have uncorrelated noise suppressed relative to any correlated component.

If we wish to observe this CSW under a source direction hypothesis, we derive the lags τ from the ray-tracing method described above. We can also find the CSW in a way that does not depend on the index of refraction model. To do this for a pair of antennas i and j , we consider all potential lags τ and choose the one that provides the highest $C_{i,j}$.

4. Correlated Thermal Noise from the Sun

We conclude that the source of the reconstruction of the events is the presence of correlated thermal noise between antennas. This is consistent with the sun acting as a bright thermal point source that illuminated all antennas. The observation that a thermal source generates fields that are correlated between spatially separated detectors is expected and understood from classical theories of statistical optics; for example, see *Goodman* [12] Chapters 5 and 6.

Thermal noise would be characterized by spectral amplitudes, in a given frequency bin, whose distribution over many events would follow Rayleigh distributions [12]. To verify this thermal nature, we looked at the spectral amplitudes for different frequency bins and attempted to fit each against a Rayleigh distribution. For a sliding three-minute time bin across the duration of the flare, we fit the distribution of spectral amplitudes x in a given frequency bin to a Rayleigh:

$$H(x) = \frac{Ax}{\sigma^2} \exp -\frac{x^2}{2\sigma^2}. \quad (4)$$

as was done to characterize the noise environment in other analyses [4, 13]. The normalization of the fit A and the characteristic width parameter σ are allowed to float.

The top panel of Fig. 6 shows two spectral amplitude distributions for 210 and 250 MHz with their best fit Rayleigh superimposed. For comparison, the bottom panel of Fig. 6 shows a set of Rayleigh distributions from February 11th, 2011 when the sun was not active. The quality of the fit is evaluated by computing the reduced χ^2 test statistic for each spectral and time bin. The distribution of the reduced χ^2 test statistic is Gaussian and

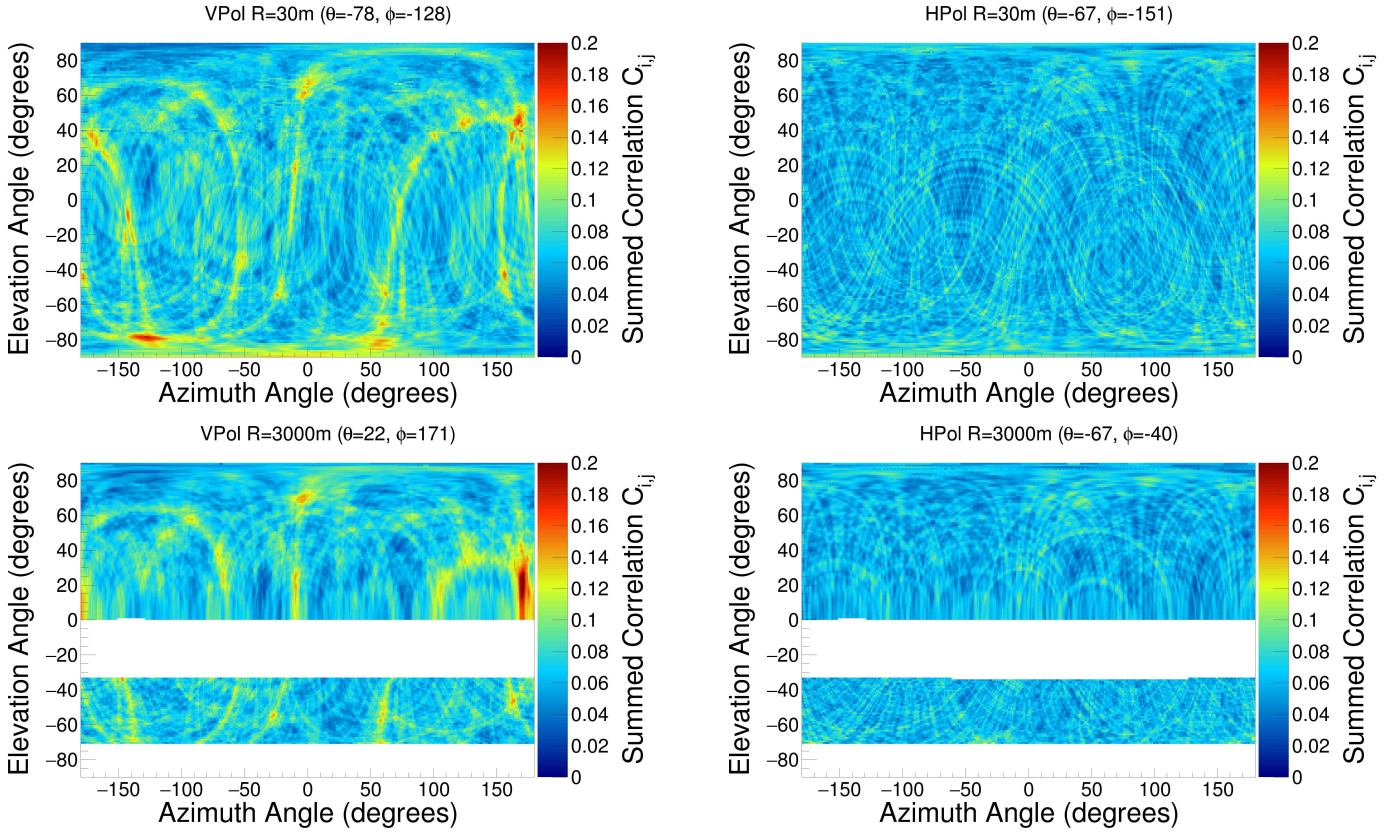


Figure 4: Map of cross-correlation values associated with directional hypotheses across the sky for the same event from the flare period as the one shown above in Figs. 8 and 10. The upper two figures show reconstruction maps for the hypothesis of 30 m distance, while the lower two figures show reconstruction maps for the 3000 m distance hypothesis. The maps are created in the Testbed local coordinate system. The white gaps in the 3000 m maps correspond to areas of ice where there is either no ray tracing solution (upper white band) or where there is bedrock (lower white band).

centered about 1 for all time bins except for the five minutes after 2:20 AM. This is shown in the bottom panel of Fig. 5 for a two-channel CSW (described below). Note that this short period coincides with a gap in the passing events that track with the Sun’s position. Note also that the σ parameter, which represents the power in a spectral bin, is higher on Feb 15 than on Feb 11, consistent with the brightened thermal emission over background observed in Sec. 3. Fits for a larger variety of frequencies on February 15th are available in Appendix 13.

In the top panel of Fig. 7, we plot the evolution of the fit parameter σ as a function of time. We find that for frequencies between 200-400 MHz, σ increases at times coincident with the brightening of the flare observed in spectrograms. Based on the quality of the single-channel fits, we find the excess power during the flare in the 200-400 MHz band to be consistent with that of thermal emission. We do not mean that the observed emission has a relationship between the intensity of spectral modes that follows a blackbody spectrum.

We also perform the Rayleigh fits for the CSWs described in Sec. 3.2, and best fit values of the σ parameter are shown as a function of time on the bottom of Fig. 7 for comparison to those derived from the single-channel fits.

These particular CSWs are formed out of only two antennas of like polarization and using the time lag that gives the highest cross-correlation value. This is likely to give us a time lag that is more appropriate for picking out the correlated component than a time lag that is derived from a directional hypothesis, given that we observe timing uncertainties associated with our directional hypotheses. By fitting Rayleigh distributions to the spectral amplitudes derived from the CSWs, we are investigating the nature of the emission that is correlated between the antennas, as the CSW suppresses the uncorrelated component relative to the correlated component. The radiation that is correlated between the antennas is also consistent with thermal, and looks similar to the distribution of total excess emission seen in a single channel in the left panel.

In the progress of determining the thermal nature of the events, we also investigated the possibility that the reconstructability of the events was due to the presence of (1) low signal-to-noise ratio transients, (2) continuous-wave (CW) contamination, (3) time-dependent features like chirps that might be expected in solar radio emission. We found evidence for only the thermal emission described in this section, though we review the findings of these other investigations in Appendix C.

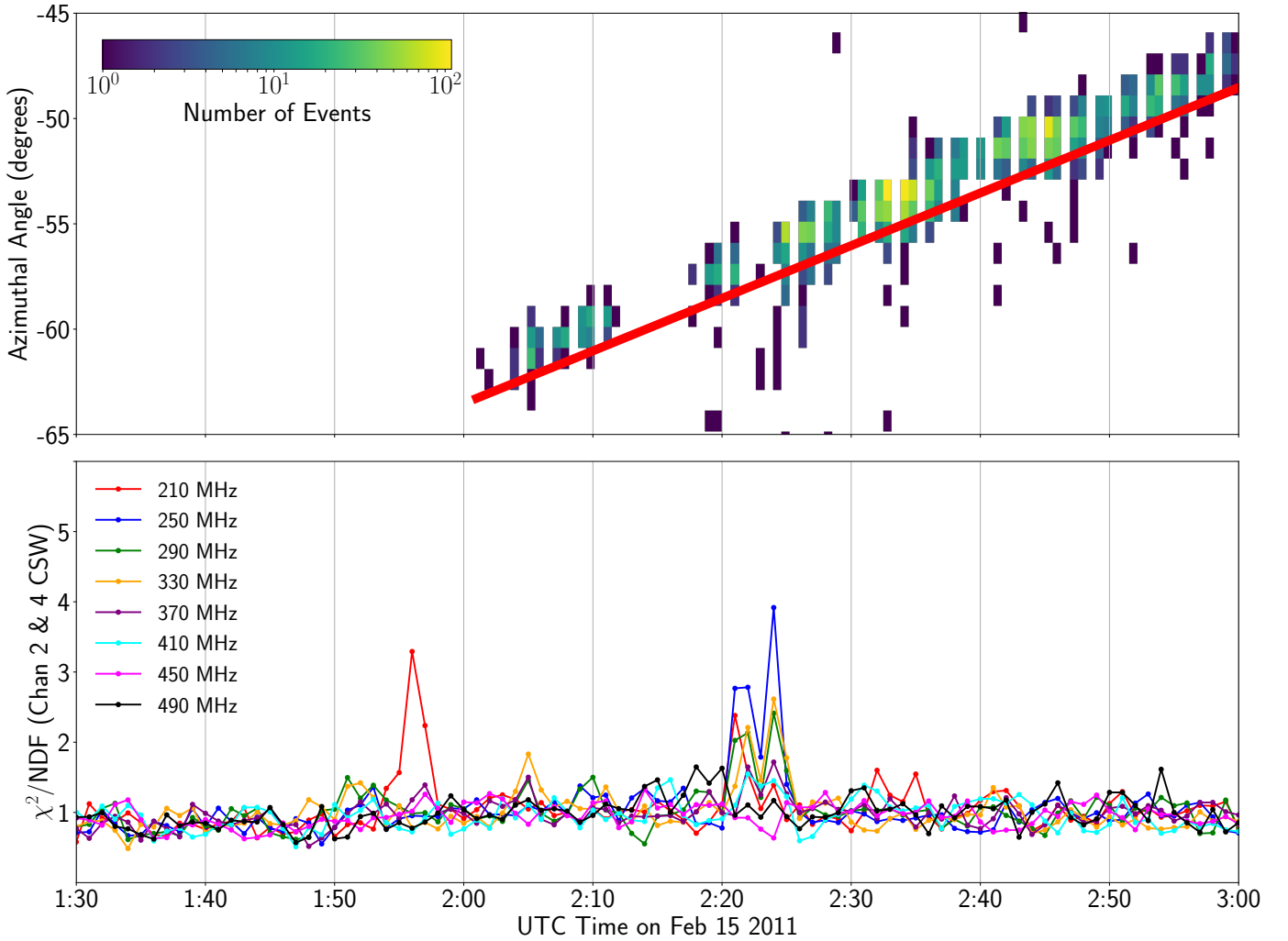


Figure 5: (Top panel) Reconstructed direction in azimuth of events occurring during the flare, and the expected location of the sun drawn as a red line. The azimuthal angle here follows the continent global coordinate system described in the Appendix. (Bottom panel) The χ^2/NDF values for fits of the spectral amplitudes to Rayleigh distributions of the CSW formed from channel 2 and 4 (see section 4) given the delay relative to one another that gives the strongest cross-correlation value. We only use two channels to avoid a reduction in the signal strength due to any timing misalignments for a given directional hypothesis. Note the increased deviation from the Rayleigh fit in the few minutes after 2:20 UTC which matches a period when the events no longer pass the analysis cuts.

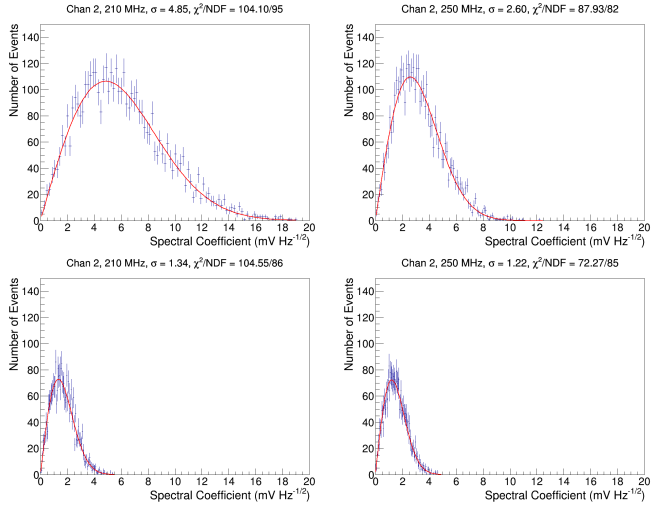


Figure 6: (Top): Distributions of amplitude spectra at two frequencies where the emission was strong, 210 MHz and 250 MHz, during the period of flare. These events satisfied the RF trigger between 1:59 and 2:01 UTC. (Bottom): The same as the top figure, but during a time when the sun was not active. These events are from the forced triggered data sample recorded on February 11th, 2011 between 01:40 and 03:00.

5. Implications

Although the detection of solar flares by ARA is not the experiment’s purpose, such events provide the opportunity to enhance the information extracted from above-ice RF sources, especially the astronomical coordinates of cosmic-ray air showers. Being sourced from the sun, the solar flare events enable validation of software used to project an event’s RF reconstruction direction onto celestial coordinates.

The power of these flare events is, at present, limited by systematic uncertainties associated with ARA reconstruction algorithms. Each antenna has both an associated surveying uncertainty and also an associated cable delay uncertainty. Additionally, there is an overall uncertainty in the details of the ice medium transporting the radio signal - specifically, the refractive index profile as well as the surface slope at the optical entry point into the ice. Once those uncertainties can be narrowed to the level of the statistical error on the ARA channel-to-channel timing cross-correlation (~ 100 ps), solar flare events can then be used to help point reconstructed ultra-high energy cosmic rays. Specifically, the solar flare data is useful because it contains many events (> 1500 events/min) which have clear reconstructions on an event-by-event basis. The sun is a true far-field plane wave emitter at a known location, and moves slowly enough to be treated as stationary while statistics accumulate, and still sweeps out a series of azimuthal angles.

Finally, if events like these are observed again, the flare can serve as a calibration source for the entire array. As future ARA stations are deployed, they will be positioned further from pulsars deployed near South Pole infrastruc-

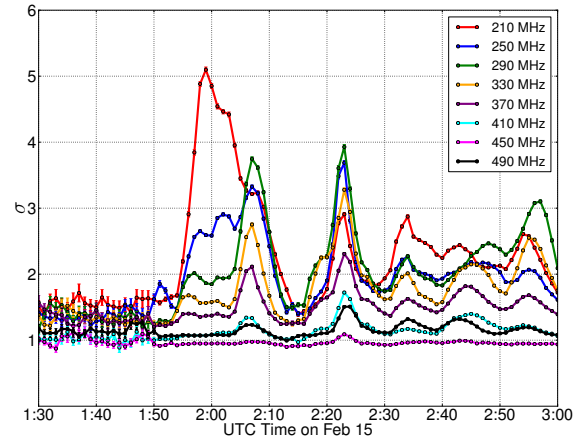


Figure 7: (Top) The time evolution of the Rayleigh fit parameter for channel two as a function of time. (Bottom) The same for the CSW from channels 2 and 4. In both, the error bars are the one-standard deviation errors on the fit parameter. The larger error bars before 1:50 are due to lower statistics before the trigger saturates after $\sim 1:50$ AM.

ture (like the pulser atop the IceCube Counting Laboratory, or “ICL rooftop pulser”). As this distance increases, the effectiveness of the ICL Pulser will diminish as the signal will be considerably weaker at the far stations. With a solar flare as a calibration source, the strength of the signal remains consistent across all stations.

6. Other Solar Flares in ARA Data

6.1. Search for Other Solar Flares with the Testbed

In addition to the Feb. 15th events found through the interferometric analysis described here, and the Feb. 13th events discussed in Appendix D, we also located bursts of radio emission coincident with three other solar flares in 2012. Events were found to correlate with solar flares from March 5 2012, March 7 2012, and Nov 21 2012.

We checked the reason these other three flares do not pass the interferometric analysis. For this purpose, we

again removed the cut which required the events come from within the ice. For the March 5 flare, no single cut is responsible for the rejection of all events. For March 7 and November 21, all events are rejected by a cut designed to remove events contaminated by continuous-wave (CW) emission; more than 86% of recorded events are also simultaneously rejected by the “Reconstruction Quality Cut” which imposes requirements on the height and size of the peak in the interferometric maps. We do not explore these events further here.

6.2. Search for Solar Flares with Deep ARA Stations

A search was performed to attempt to detect similar solar flare emission in the deep stations around the times of the X-class solar flares listed in table 1 in Appendix D. In examining data from one of the deep stations (A2) taken during the 2013 season (data already analyzed for purposes of a diffuse search [13]), the cut criteria were altered to attempt to identify clusters of events that reconstruct to the Sun’s position. Because of the differences between the Testbed station and the deep station, the same set of cuts were not used but rather only one cut was implemented: the event must have a reconstructed correlation value greater than 0.18 with a assumed reconstruction radius of 3000 m. To test the validity of this method’s ability to reconstruct events above the ice, it was applied to ICL rooftop pulser events (described in Sec. A.3), which reconstructed regularly to the correct position above the ice. After applying this cut on the data taken during the 2013 solar flare periods, we find no events passing these cuts. However, this search was not explicitly designed to detect solar events, and it is also the case that ARA has yet to analyze data from 2014 forward, which was a more active part of the solar cycle than 2013 [14], and so some deep station cases may still be in archival data.

7. Conclusions and Discussion

The ARA Testbed has recorded events during a solar flare on February 15th, 2011 that contain a broadband signal and uniquely and tightly reconstruct within a few degrees of the Sun. The excess radio emission is found to contain a component that is coherent across the antennas, consistent with correlated thermal emission expected from the sun being a bright thermal point source.

This is the first observation by ARA, and by an ultra-high energy Antarctic radio neutrino telescope, of emission that can be identified as being produced at an extraterrestrial source on an event-by-event basis. The events offer a high statistics data set that, coupled with improved systematic uncertainties, can validate the software ARA uses to map above-ice RF sources, such as cosmic-ray air showers, to celestial coordinates.

From the perspective of solar physics, we offer a comparison of spectrograms derived from the total observed emission and compare to the spectrograms obtained with

the correlated component amplified. This may provide a view of the mechanisms through which the correlated and uncorrelated components of the emission are produced. On a basic level, due to our 2 GHz sampling of 250 ns waveforms, ARA may be able to contribute to the knowledge of solar flare phenomena on smaller time scales than can be probed elsewhere, and thus smaller length scales.

ARA’s location in the southern hemisphere and radio quiet environment may add data to the worldwide network of solar burst spectrometers. At present, most spectrometers are located in the Northern Hemisphere (e.g. Greenbanks in Virginia, Palehua in Hawaii, Ondrejov in the Czech Republic). Some reside in the south—for example, Culgoora and Learmouth—but are contaminated by steady-state man-made spectral features, for example the noise lines in Culgoora spectrographs near 180 and 570 MHz. The radio community has already expressed a need for a so-called “Frequency Agile Solar Radiotelescope” [7], to which ARA bears remarkable resemblance in bandwidth and digitization electronics. This could also be true for other radio neutrino-telescopes deployed to Antarctica, such as ARIANNA [15].

8. Acknowledgements

We thank the National Science Foundation for their generous support through Grant NSF OPP-902483 and Grant NSF OPP-1359535. We further thank the Taiwan National Science Councils Vanguard Program: NSC 92-2628-M-002-09 and the Belgian F.R.S.-FNRS Grant 4.4508.01. We are grateful to the U.S. National Science Foundation-Office of Polar Programs and the U.S. National Science Foundation-Physics Division. We also thank the University of Wisconsin Alumni Research Foundation, the University of Maryland and the Ohio State University for their support. Furthermore, we are grateful to the Raytheon Polar Services Corporation and the Antarctic Support Contractor, for field support. B. A. Clark thanks the National Science Foundation for support through the Graduate Research Fellowship Program Award DGE-1343012. A. Connolly thanks the National Science Foundation for their support through CAREER award 1255557, and also the Ohio Supercomputer Center. A. Connolly, H. Landsman, and D. Besson thank the United States-Israel Binational Science Foundation for their support through Grant 2012077. A. Connolly, A. Karle, and J. Kelley thank the National Science Foundation for the support through BIGDATA Grant 1250720. K. Hoffman likewise thanks the National Science Foundation for their support through CAREER award 0847658. D. Z. Besson and A. Novikov acknowledge support from National Research Nuclear University MEPhI (Moscow Engineering Physics Institute). R. J. Nichol thanks the Leverhulme Trust for their support.

We would finally like to thank Dan Gauthier, John Beacom, Kenny Ng, Dale Gary, and Nita Gelu for helpful discussions.

9. Bibliography

- [1] G. A. Askaryan, Excess Negative Charge of an Electron-Photon Shower And Its Coherent Radio Emission, *JETP* 14 (1962) 441.
- [2] G. A. Askaryan, Coherent Radio Emission from Cosmic Showers in Air and in Dense Media, *JETP* 21 (1965) 658.
- [3] P. Allison, et al., Design and Initial Performance of the Askaryan Radio Array Prototype EeV Neutrino Detector at the South Pole, *Astroparticle Physics* 35 (2012) 457–477. [arXiv: 1105.2854](https://arxiv.org/abs/1105.2854), doi:10.1016/j.astropartphys.2011.11.010.
- [4] P. Allison, et al., First constraints on the ultra-high energy neutrino flux from a prototype station of the askaryan radio array, *Astroparticle Physics* 70 (2015) 62 – 80. doi:<http://dx.doi.org/10.1016/j.astropartphys.2015.04.006>. URL <http://www.sciencedirect.com/science/article/pii/S0927650515000687>
- [5] Rhessi flare list, <https://hesperia.gsfc.nasa.gov/rhessi3/data-access/rhessi-data/flare-list/index.html>, accessed: 2017-05-13.
- [6] S. M. White, Solar Radio Bursts and Space Weather, *Asian Journal of Physics* 16 (2007) 189–207.
- [7] Z. Liu, D. E. Gary, G. M. Nita, S. M. White, G. J. Hurford, A subsystem test bed for the frequency agile solar radiotelescope, *Publications of the Astronomical Society of the Pacific* 119 (853) (2007) 303. URL <http://stacks.iop.org/1538-3873/119/i=853/a=303>
- [8] Fermi solar flare x-ray and gamma-ray observations, https://hesperia.gsfc.nasa.gov/fermi_solar/, accessed: 2017-05-13.
- [9] Sws - culgoora observatory - type ii events, <http://www.sws.bom.gov.au/Solar/2/5/1>, accessed: 2017-05-12.
- [10] I. Kravchenko, D. Besson, J. Meyers, In situ index-of-refraction measurements of the South Polar firn with the RICE detector, *Journal of Glaciology* 50 (2004) 522–532. doi:10.3189/172756504781829800.
- [11] M. Lu, C. Pfendner, A. Shultz, Ultra-high energy neutrino search with the askaryan radio array, *Proceedings of Science (ICRC2017)*. URL <https://pos.sissa.it/301/966/pdf>
- [12] J. Goodman, *Statistical Optics*, 1985.
- [13] P. Allison, et al., Performance of two Askaryan Radio Array stations and first results in the search for ultrahigh energy neutrinos, *Phys. Rev. D* 93 (8) (2016) 082003. [arXiv:1507.08991](https://arxiv.org/abs/1507.08991), doi:10.1103/PhysRevD.93.082003.
- [14] Noaa space weather prediction center, solar cycle progression, <https://www.swpc.noaa.gov/products/solar-cycle-progression>, accessed: 2018-05-12.
- [15] S. W. Barwick, et al., Design and Performance of the ARI-ANNA HRA-3 Neutrino Detector Systems, *IEEE Trans. Nucl. Sci.* 62 (5) (2015) 2202–2215. [arXiv:1410.7369](https://arxiv.org/abs/1410.7369), doi:10.1109/TNS.2015.2468182.
- [16] P. W. Gorham, et al., The Antarctic Impulsive Transient Antenna Ultra-high Energy Neutrino Detector Design, Performance, and Sensitivity for 2006–2007 Balloon Flight, *Astropart. Phys.* 32 (2009) 10–41. [arXiv:0812.1920](https://arxiv.org/abs/0812.1920), doi:10.1016/j.astropartphys.2009.05.003.
- [17] Plataforma solar de almeria sun position algorithm, <http://www.psa.es/sdg/sunpos.htm>, accessed: 2017-01-15.
- [18] M. Blanco-Muriel, D. C. Alarcón-Padilla, T. López-Moratalla, M. Lara-Coira, Computing the solar vector, *Solar Energy* 70 (5) (2001) 431 – 441. doi:[http://dx.doi.org/10.1016/S0038-092X\(00\)00156-0](http://dx.doi.org/10.1016/S0038-092X(00)00156-0). URL <http://www.sciencedirect.com/science/article/pii/S0038092X00001560>
- [19] M. R. Kundu, *Solar Radio Astronomy*, 1965.
- [20] M. J. Reiner, M. L. Kaiser, J. Fainberg, J.-L. Bougeret, R. G. Stone, Remote Radio Tracking of Interplanetary CMEs, in: A. Wilson (Ed.), *Correlated Phenomena at the Sun, in the Heliosphere and in Geospace*, Vol. 415 of *ESA Special Publication*, 1997, p. 183.
- [21] Stereo / waves science investigation, https://swaves.gsfc.nasa.gov/swaves_science.html, accessed: 2017-05-12.
- [22] M. Aschwanden, *Physics of the Solar Corona*, 2005.
- [23] J. P. Wild, Observations of the spectrum of high-intensity solar radiation at metre wavelengths. ii. outbursts, *Australian Journal of Scientific Research A* 3 (1950) 399.
- [24] J. Meléndez, H. Sawant, F. Fernandes, A. Benz, Statistical analysis of high-frequency decimetric type iii bursts, *Solar Physics* 187 (1999) 77–88.
- [25] A. R. Jacobson, S. O. Knox, R. Franz, D. C. Enemark, Forte observations of lightning radio-frequency signatures: Capabilities and basic results, *Radio Science* 34 (2) (1999) 337–354. doi:10.1029/1998RS900043.
- [26] K.-S. Cho, et al., A high-frequency type II solar radio burst associated with the 2011 February 13 Coronal Mass Ejection, *Astropart. Phys.* 765 (2013) 148–156. doi:doi:10.1088/0004-637X/765/2/148.

Appendices

A. Supporting Figures

A.1. Waveforms and Spectra

Fig. 8 shows waveforms from an event at 02:04 GMT, near the beginning of the flare period. For comparison, in Fig. 9 we show a typical event from February 11, 2011, four days before the flare of interest when the sun was not active. Figs. 10 and 11 show corresponding spectral amplitudes, from the Fourier transforms of the waveforms in the previous two figures.

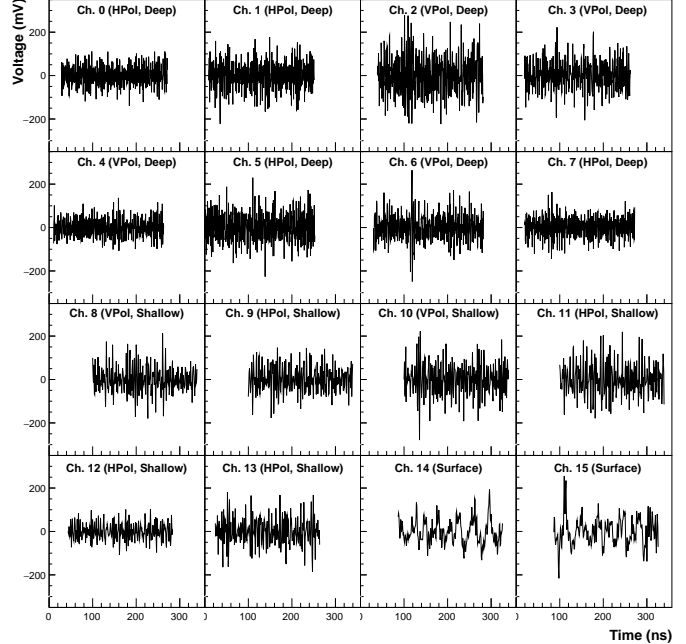


Figure 8: Example waveform for a typical event during the flare period, recorded at 02:04, Feb 15th 2011 UTC.

A.2. Rayleigh Fits

An example of fits for four borehole antennas is given in Fig. 12 and the fit to the CSW of those four boreholes is

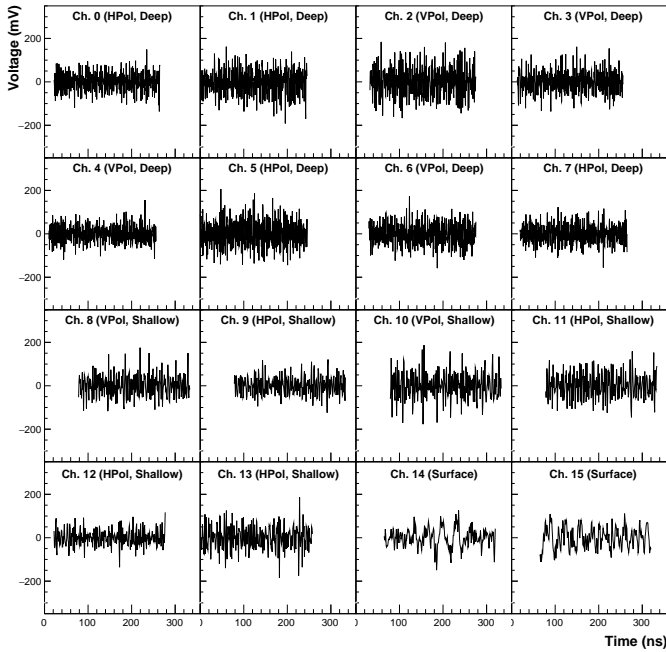


Figure 9: Example waveforms for a typical non-flare event, recorded at 02:04, Feb 11th 2011 UTC.

given in Fig. 14. This demonstrates again that the single channel spectra, and the CSW, are both thermal in nature.

We also show in figure 13 spectral amplitude distribution and their associated Rayleigh fits for a broader selection of frequencies.

A.3. Polarization

As seen in Fig. 4, we find higher peak cross-correlation values from waveforms from VPol antennas than from the HPol antennas. We decided to investigate whether this VPol dominance had originated in the sun, or rather was due to higher gains in VPol antennas than HPol antennas. Although some solar flares do emit radio that is circularly polarized—thought to be associated with how plasmas generating the radio emission orient themselves with respect to dynamic magnetic field lines—we would expect it to be a coincidence if the emission would happen to prefer the vertical direction at the site of the ARA Testbed.

In order to measure the relative response of the VPol and HPol antennas in the Testbed *in situ*, we used recorded waveforms from a pulser mounted to the top of the Ice-Cube Counting Laboratory (ICL) at the South Pole, nicknamed the “ICL Pulser.” This is a Seavey broadband ($\sim 200 - 1200$ MHz), dual-polarized quad-ridged horn antenna, the same as is used for the ANITA payload [16], that transmits pulses in both polarizations. The ICL Pulser sits 2.1 km from the Testbed at a 13 m height, so that the pulse destined for a Testbed antenna would approach the ice at approximately $\sim 0.36^\circ$ above the surface. This Seavey antenna is ideally suited for this measurement because its response across the band is very similar in both polarizations [16].

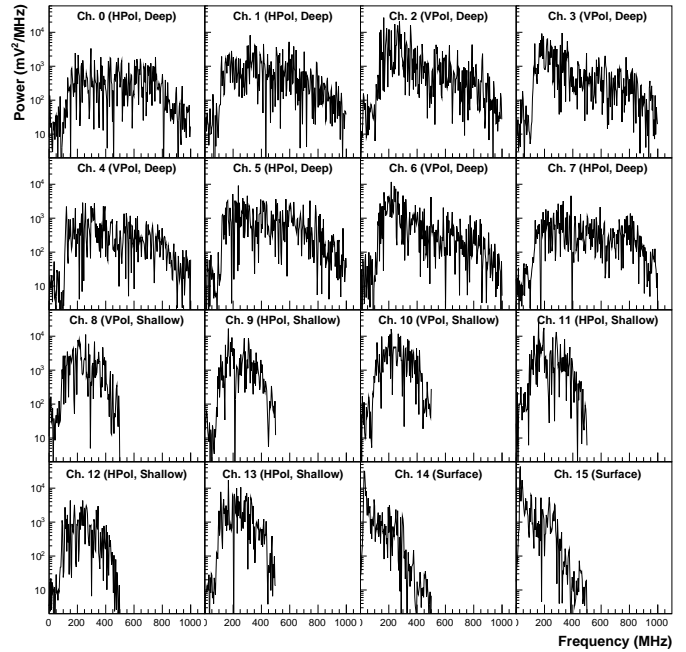


Figure 10: Example amplitude spectra for the same event during the flare as in Fig. 8, recorded at 02:04, Feb 15th 2011 UTC.

For this study, we used ICL Pulser data taken on January 26th, 2013, during two different forty-minute long runs where the pulser was either transmitting in VPol or HPol mode. We use forty events in each run where we found the highest cross-correlation value for a direction within 10° in azimuth of the expected ICL Pulser position and a zenith angle above the surface. We take the Fourier Transform of each waveform and, for each antenna, average the spectral amplitudes for the forty events in a run.

We use the following procedure to measure the frequency-dependent ratio of HPol to VPol spectral amplitudes. We considered pairs of antennas that were deployed in the same borehole and within 3-6 m of each other in depth, and for each pair, took the ratio of the average spectral amplitudes measured in the HPol during HPol transmission mode to the average spectral amplitudes measured in the VPol during VPol transmission mode, after accounting for the different Fresnel coefficients governing the fraction of field-amplitude transmitted at the air-ice boundary for each polarization, t_H and t_V . For the 89.64° angle with respect to normal at air-to-ice interface, the transmission coefficients are $t_V = 0.0185$ for VPol signals and $t_H = 0.0138$ for HPol signals using an index of refraction at the surface of 1.35. The four ratios are then averaged together.

To compute the Fresnel coefficients for the antenna calibration, we assume that the ICL roof-top pulser is 13.16m above the ice at a distance of 2099.06m away (accounting for differences in ice elevation at the location of Testbed and the ICL). This leads to a angle from the surface of $\theta_{pulser} = \tan^{-1}(\frac{13.16\text{m}}{2099.06\text{m}}) = 0.36^\circ$ or 89.64° from surface normal.

The transmission coefficient in *voltage* for the polariza-

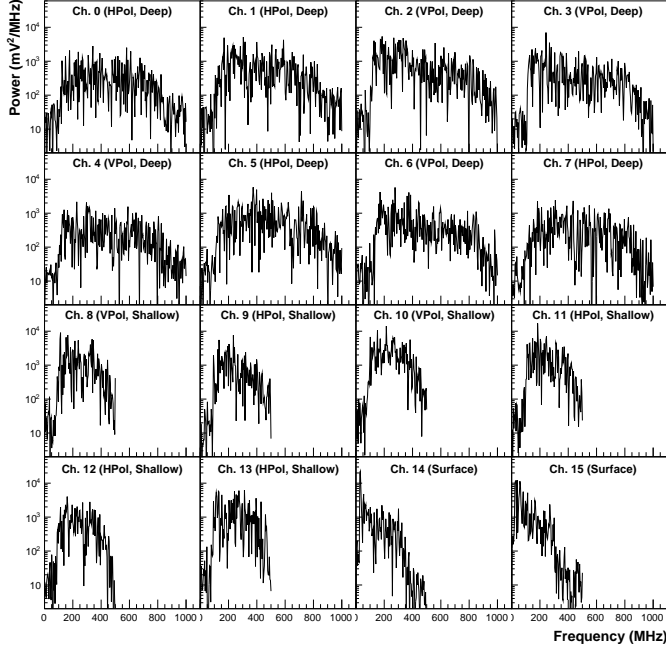


Figure 11: Amplitude spectra for the same typical event in Fig. 9 from a time where the sun was quiescent, at 02:04, Feb 11th UTC.

tion parallel to the normal (perpendicular or the surface of the ice, our VPol) is given by t_V :

$$t_V = \frac{2n_{\text{air}} \cos \theta_i}{n_{\text{air}} \cos \theta_t + n_{\text{fim}} \cos \theta_i} = \frac{2 \sin \theta_t \cos \theta_i}{\sin(\theta_i + \theta_t) \cos(\theta_i - \theta_t)} \quad (5)$$

The transmission coefficient in *voltage* for the polarization perpendicular to the normal (parallel to the surface of the ice, our HPol) is given by t_H :

$$t_H = \frac{2n_{\text{air}} \cos \theta_i}{n_{\text{air}} \cos \theta_i + n_{\text{fim}} \cos \theta_t} = \frac{2 \sin \theta_t \cos \theta_i}{\sin(\theta_i + \theta_t)} \quad (6)$$

where $n_{\text{air}} = 1$ is the index of refraction in air, $n_{\text{fim}} = 1.35$ is the assumed index of refraction in the shallow ice, θ_t is the transmission angle with respect to normal, and θ_i is the incidence angle with respect to normal, and the relationship between θ_t and θ_i is found by Snell's law.

For the solar flare sample—namely all 2323 events passing cuts— we first build coherent sums of every event in both polarizations. The coherent sum waveforms are then Fourier transformed and averaged, accounting for Fresnel coefficients for the incidence angle of the sun (which is 13.3 ° above the surface). The ratio of the spectral averages is then corrected by the known relative antenna responses found through the ICL calibration procedure above. Fig. 16 summarizes the results of this investigation of the polarization of the flare emission. The plots show (left) that for these shallow incidence angles, the HPol antenna response is intrinsically weaker than the VPol antenna response across the band from ~220 MHz to 500 MHz by about a factor of three, and that (right) once this is accounted for, the emission from the flare is consistent

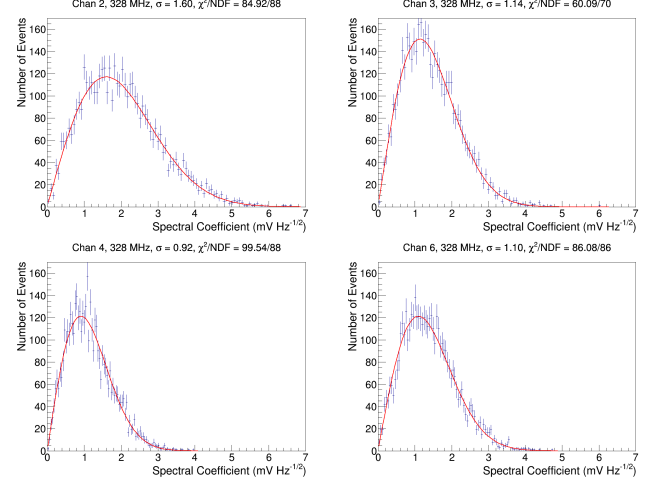


Figure 12: Distribution of spectral amplitudes at 328 MHz for the four borehole VPol antennas in the Testbed.

with having equal contributions in HPol and VPol. The anomalies at ~150 MHz are likely due to a difference in the gains of the two types of antennas in this region, and can be seen as a calibration artifact in the left panel.

B. Coordinate Systems

B.1. Solar Coordinates

The location of the sun is computed with a publicly available C library [17] developed by the Platforma Solar de Almería (PSA). For a given unixtime, latitude, and geographic longitude, the program returns the position of the sun (both azimuth and zenith angle) to within 0.5 arcminutes. The PSA algorithm is chosen for its simplicity of implementation while preserving sub-degree solar position accuracy for the years 1999-2015 [18].

The PSA method returns the sun location in a coordinate system where zero in azimuth is defined by the meridian of the observer, in this case, the longitude of the prototype station, which is 74.22° W from Prime Meridian (rounded to the nearest hundredth). We first rotate this reported value to align with the geographic grid of the South Pole, where zero azimuth is defined by the Prime Meridian. This “continent” coordinate system natively follows a *clock-wise* convention where N(orth) = 0° = Prime Meridian, E(ast) = 90°, S(outh) = 180°, and W(est) = 270°. We further transform coordinate systems to one which proceeds *counter-clockwise* in the physics tradition, so E = 0°, N = 90° = Prime Meridian, W = 180°, and S = 270°. We finally rescale the azimuth range from [0, 360] to [-180, 180] to match the output of the analysis interferometric map methods described in section B.2. The result is that the solar azimuth is reported as a counter-clockwise angle in the range of [-180, 180] in a coordinate system where E = 0°, N = 90° = Prime Meridian, W = 180°, and S = -90°.

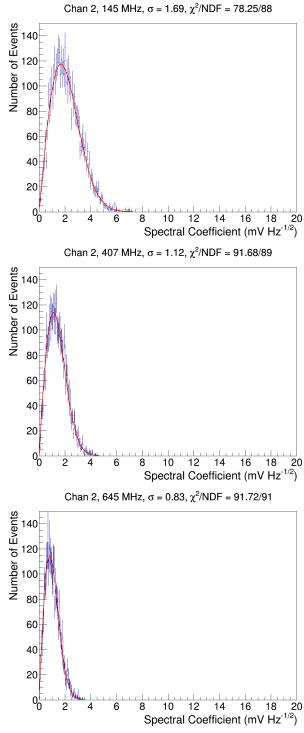


Figure 13: A selection of spectral amplitudes for several frequencies across our band with their best fit Rayleigh’s superimposed.

B.2. Interferometric Map Coordinates

The interferometric map measures azimuthal angles in a counter-clockwise coordinate system with zero azimuth corresponding to the direction of Antarctic continent ice-flow. At the location of the prototype station, this corresponds to 36.77° W from Prime Meridian (rounded to the nearest hundredth). We rotate the map by this constant offset to align the map with the same “continent” coordinate system as used for solar positions in section B.1, so that $E = 0^\circ$, $N = 90^\circ$ = Prime Meridian, $W = 180^\circ$, and $S = -90^\circ$. The interferometry routines are already designed to report answers in the range of $[-180, 180]$ as in [4], so unlike the PSA routine, a range adjustment is not required.

B.3. A note On Convention Selection

We note that the azimuthal (ϕ) coordinate system utilized here ($E = 0^\circ$, $N = 90^\circ$ = Prime Meridian, $W = 180^\circ$, and $S = -90^\circ$) is 90° out of phase with the ISO 6709 definition of longitude. It does however agree with the methodology used by South Pole surveyors in determining coordinates for both ARA and IceCube.

C. Other Hypotheses For Unique Reconstruction to the Sun

We concluded, as described in the main body of the paper, that the events were consistent with bright thermal emission. In this Appendix, we detail other studies

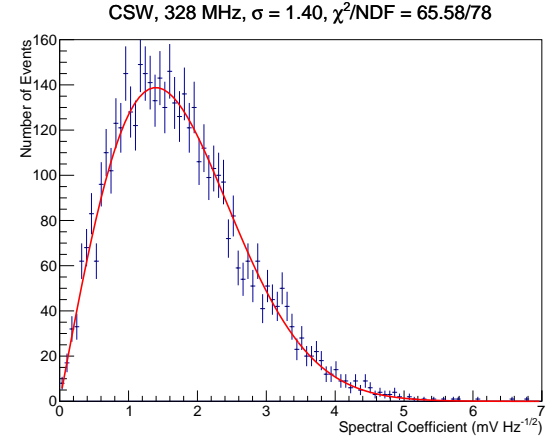


Figure 14: Distribution of spectral amplitudes at 328 MHz for the coherently summed waveform derived from the four borehole VPol antennas in that are shown in Fig. 12. The CSW is made with directional hypothesis time lags corresponding to the correlation peak on the map for a given event.

we undertook to explicitly rule out the hypotheses of CW emission, low signal-to-noise transients, broad-band but non thermal emission produced by solar flares.

C.1. Continuous Wave

We looked for evidence of the emission being CW-like by looking for a strong peak or peaks at unique frequencies in the spectra. Any impulse whose duration would be shorter than our waveforms of ~ 250 ns in length when produced at the sun would be dispersed over several μ s in the ionosphere, so we looked for a chirp-like behavior in the waveforms.

Continuous wave signal at frequencies higher than $\sim 1/200\text{ns} = 5$ MHz will repeat over timescales less than ~ 200 ns. The ARA Testbed high-pass filters remove frequencies below 150 MHz, so the unique reconstruction to the sun that we are seeing cannot be due to signals being at sufficiently low frequencies that their period is not contained in our waveforms. Fig. 17 shows a reconstruction map from continuous wave interference at ~ 403 MHz (the radiosonde on South Pole weather balloons), where one can see peaks in the cross-correlation function corresponding to directions all over the map.

C.2. Transients

Any signal that only begins, or ceases, to be observed at some time between the beginning and end of the waveforms would also give a unique reconstruction direction. For example, impulsive signals reconstruct cleanly, as demonstrated from a measured calibration pulser in Fig. 17. However, any impulsive signal that might be produced by the flare would be dispersed as it exits the sun as well as in the earth’s ionosphere.

To check whether the cause of the unique reconstruction of these events to the sun was some emission with

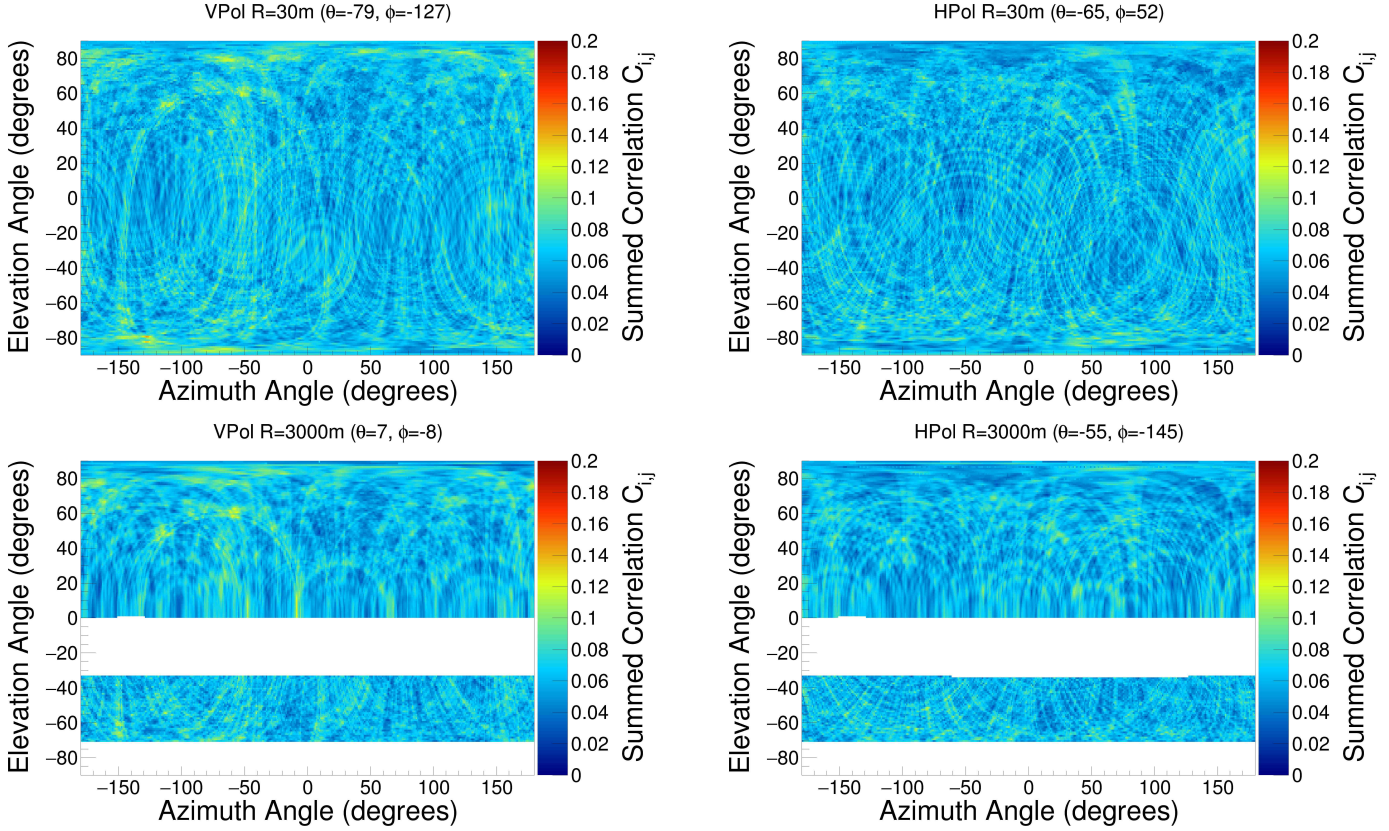


Figure 15: Map of cross-correlation values associated with directional hypotheses across the sky for the same event from a time when the sun was quiescent as the one shown above in Figs. 9 and 11. The upper two figures show reconstruction maps for the hypothesis of 30 m distance, while the lower two figures show reconstruction maps for the 3000 m distance hypothesis. The maps are created in the Testbed local coordinate system.

start or end times observed in our waveforms, we considered the channel with the largest peak voltage compared to the RMS noise voltage, and divided up the waveforms in the event into three sections: an 80 ns window surrounding the time of the peak, and the periods before and after that window (See Fig. 18). The windows in the waveforms from each antenna are delayed to be consistent with the Sun’s direction so that the windows in each waveform correspond with each other. As seen in Fig. 19, we find that the event reconstructs uniquely to the sun using any of the three time periods on their own. The same test applied to a calibration pulser event shows a strong reconstruction using only the “impulsive” part of the waveform and no reconstructability to the calibration pulser’s direction using the segments before and after the impulsive portion. This suggests that the signal correlated with the solar flares is not impulsive in nature but rather that the signal correlating with the Sun’s direction is spread across the waveform.

C.3. Broadband, non thermal

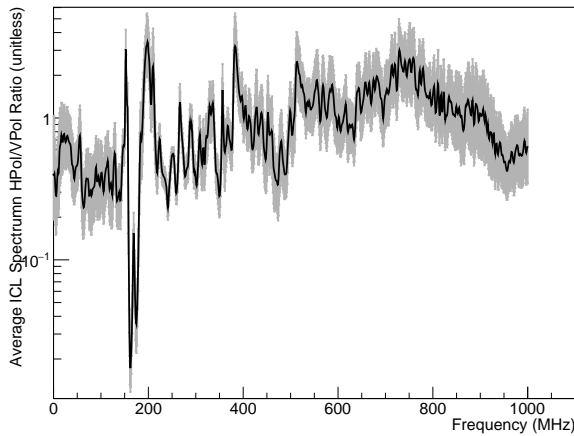
C.3.1. Time-dependent spectral features expected from solar flares

Some decimeter-wavelength (decimetric) radio emission associated with solar flares is due to excitations of the coronal plasma at the plasma frequency f_p [19]. This plasma

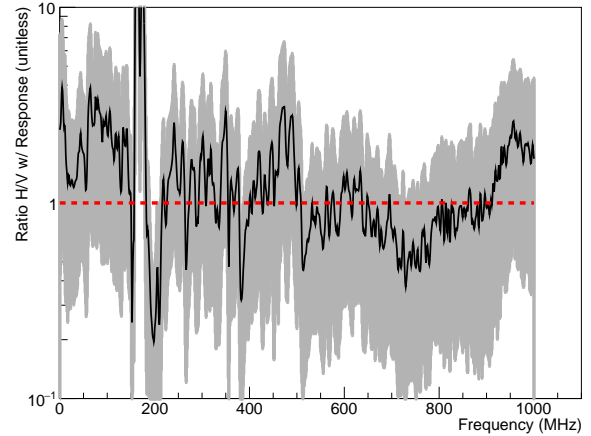
frequency depends on the square root of the electron density n_e , so that $f_p \propto \sqrt{n_e}$. The coronal electron density is in turn proportional to the inverse-square of the distance from the sun’s center R so that $n_e \propto 1/R^2$ [20, 21]. Therefore, as the electrons in the ejecta plasma are carried outward from the sun, the coronal density falls as $1/R^2$, leading to a chirp from higher to lower frequencies. This chirp is characterized by its so-called “frequency drift rate” df/dt , where $df/dt > 0$ indicates the electrons are being ejected from the sun, and $df/dt < 0$, or “reverse drift”, indicates they are being dragged back in.

The drift rate is a measure of how quickly the density of the solar atmosphere changes from the perspective of an ejecting electron and divides flares with plasma emission into two categories [22], type-II and type-III¹. The faster the ejecta, the more quickly the change in the plasma frequency, and the greater the magnitude of the frequency drift rate. Type-II flares are characterized by df/dt on the order of 10^{-1} MHz/s, and are usually attributed to

¹The numbering on the flare types is arbitrary and historical. At the time of naming, type-II flares were “slow-drift” bursts, and type-III were “fast-drift bursts”, referring to the time scale of the frequency drift. Type-I flares were “noise-storms”, type-IV were “broadband-continuum emission,” and type-V were “continuum emission at meter wavelengths.”



(a) H/V ratio of the Antenna Response



(b) H/V ratio of the solar flare spectra

Figure 16: (a) The antenna response of HPol antennas in ARA Testbed compared to that of VPol antennas, showing that the HPol antennas have lower gains by about a factor of three. (b) The observed emission from the solar flare in VPol and HPol after accounting for the different gains from the two types antennas, showing that the observed emission during the flare was consistent with being observed equally in horizontal and vertical polarizations. Note the artifact around 150 MHz is related to the calibration and is visible in the left figure, and not due to the solar flare emission.

magneto-hydrodynamic shocks (shock waves in the solar plasma excited by the evolving magnetic fields) moving through the solar corona [23]. Type-III flares drift significantly faster, upwards of 10^3 MHz/s [24], and are caused by electrons traveling outward along open field lines at speeds upward of $0.5c$.

C.3.2. Looking for features in spectrograms

The time scales of the chirps from both types of flares are orders of magnitude too long to be observable on our individual waveforms of length ~ 250 ns, and cannot explain the correlation that we are seeing between waveforms on an event by event basis. In our bandwidth (approximately 125-850 MHz), the fastest drift rates are those associated with type-III flares. Melendez *et. al.* [24] suggest that for our center frequency of 350 MHz, $df/dt \sim 700$ MHz/s, which would generate roughly 170 Hz of drift over the waveform. Such a chirp should only be visible on a timescale of $\sim 1/170\text{Hz} \sim 6$ ms, which is over 10,000 times longer than our waveform.

Impulsive events with time-scales of nanoseconds would be dispersed in the ionosphere due to the electron plasma frequency resonance in the 10-100 MHz range –as has been observed by other impulsive radio experiments like FORTE [25]. The ionospheric plasma frequency is even greater during active solar periods thus producing an even greater dispersive effect with group delays potentially reaching $1\mu\text{s}$ at 300 MHz. Therefore, if we were seeing the effect of impulsive signals that were of $\sim\text{ns}$ or 10’s of ns duration when produced at the sun, one may expect to find a chirp on the scale of 10’s to 100’s of nanoseconds. Because of the 25-ms deadtime between triggered events, μs -scale and ms-scale spectrograms cannot be obtained. However, we can still

check for features in spectrograms from a single event over a 250 ns time scale, and using ~ 50 events we can produce spectrograms over timescales of order a second.

Using ~ 50 events, we can produce second-scale spectrograms, an example of which can be seen in Fig. 20. No clear pattern emerges from these spectrograms.

By examining subsections of each event, we produce event spectrograms, which demonstrate no clear chirp-like behavior on the time-scale of the event length (~ 250 ns). We divide each waveform into many segments and calculate the spectrum for each segment. Although the frequency resolution is made coarser by this process than when analyzing the full waveform, it allows the examination of the power spectrum as a function on time during the period covered by the waveform.

We confirm the absence of single-waveform chirp behavior by plotting spectrograms for single waveforms as in Fig. 21.

D. Other solar flares during the ARA livetime

In order for ARA to observe radio emission from a solar flare during the livetime of the instrument, the sun should be up in Antarctica (from mid-September to mid-March only, and 24 hours per day during that period), the flare must face the earth. Table 1 summarizes other X-class flares that satisfied the above criteria for the ARA Testbed and three deep stations from 2011 to 2013 using the RHESSI flare catalog.

D.1. The Feb. 13th solar flare reported by ARA

The ARA team observed emission from an M-class flare in the ARA Testbed that occurred on Feb. 13th, 2011, just

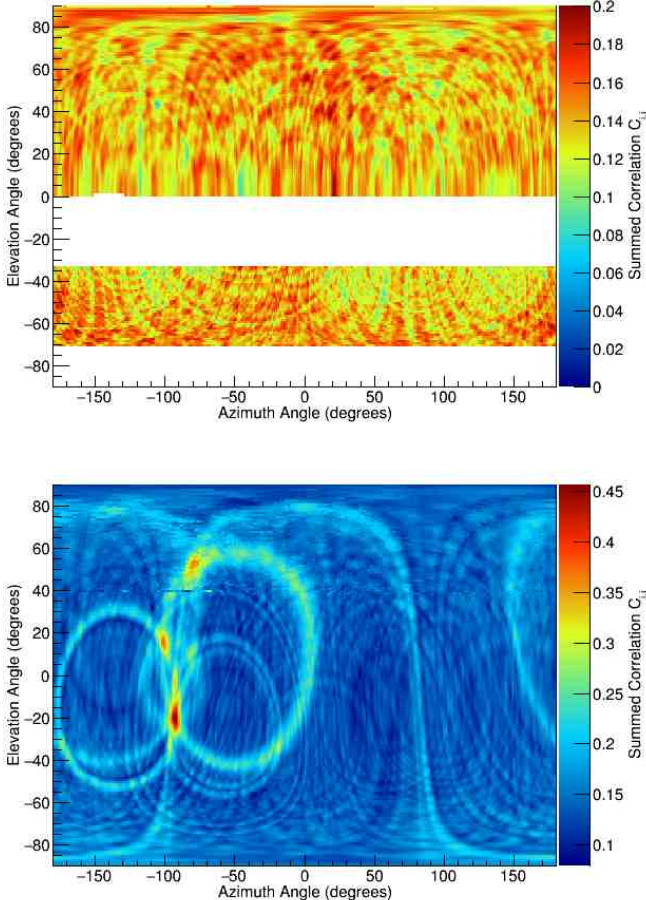


Figure 17: (Top) Reconstruction map from known continuous wave interference at ~ 403 MHz (the radiosonde on South Pole weather balloons), showing peaks in the cross-correlation function for time delays corresponding to many different directions. The behavior differs from the reconstruction maps seen for the flare as shown in Fig. 4. The map was made assuming a source distance of 3000m, and the angles are all in the local Testbed coordinate system. (Bottom) Reconstruction map from an impulsive waveform from an in-ice calibration pulser. The map was made assuming a source distance of 30m, and the angles are all in the local Testbed coordinate system.

two days before the flare that was the subject of this paper, and reported it in a paper about the performance of the Testbed instrument in 2011 [3]. This Feb. 13th flare was sought by ARA analyzers after the Green Bank Solar Radio Burst Spectrometer detected a series of strong type-II solar radio bursts in the 10 MHz-1 GHz band [26]. ARA reported a spectrogram from the Feb. 13th flare with many features similar to ones in the spectrogram report by Green Bank, demonstrating that the ARA Testbed system was sensitive to low-level radio emission, and also that the noise environment of the South Pole ARA site is sufficiently quiet to allow for such a detection.

The Feb. 13th and Feb. 15th flares had many differing characteristics that account for the different circumstances under which ARA analyzers encountered the two events. The emission from the Feb. 13th flare peaked at

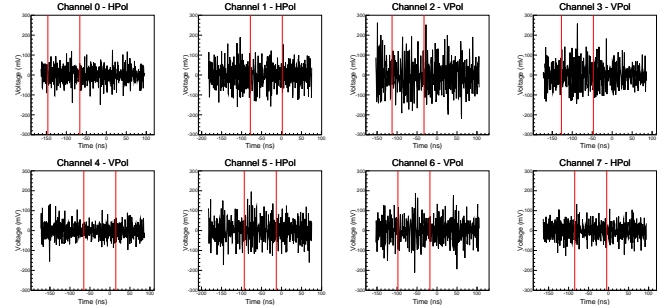
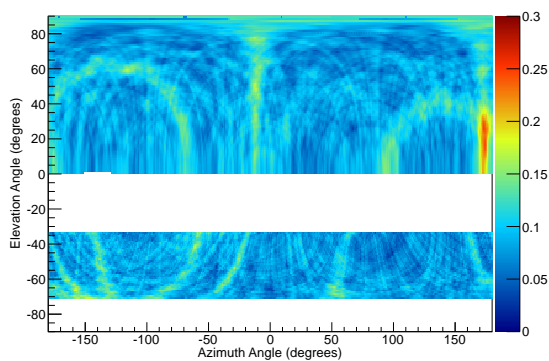


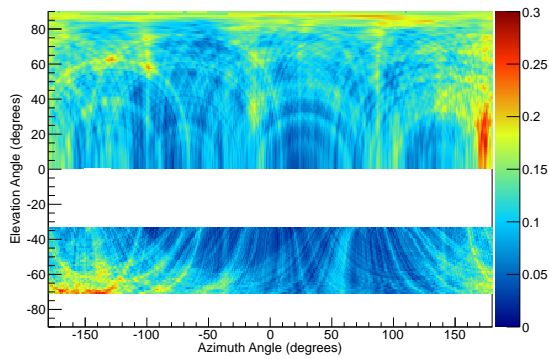
Figure 18: The waveforms from an event that reconstructs to the Sun's direction. To test whether the reconstruction is caused by an impulsive signal, the impulsive portion is defined by identifying the largest V_{peak}/RMS values across all channels contributing to the map (i.e. VPol borehole antennas) and selecting an 80-ns window around that time. For other channels, the window is defined by shifting the window in the peak waveform by the delay consistent with the peak reconstruction direction. The “impulsive” period is shown as the region between the red vertical lines.

Date	Time	Class
2011/02/15	01:43:44	X2.2
2011/03/09	23:10:28	X1.5
2011/09/22	10:53:16, 11:06:40, 11:36:04	X1.4
2011/09/24	09:19:28, 9:30:00	X1.9
2012/03/05	02:41:48, 03:12:20, 03:16:28, 03:56:04	X1.1
2012/10/23	03:14:36	X1.8
2013/10/25	07:52:44	X1.7
2013/10/25	14:56:16	X2.1
2013/10/28	01:45:24, 01:51:44	X1.0

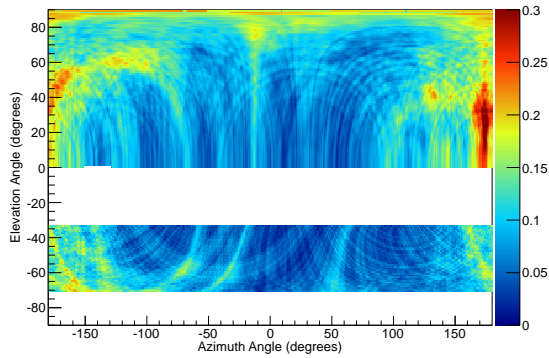
Table 1: Table summarizing X-class flares during the livetime of the ARA Testbed and three deep stations and the periods when the Sun is above the horizon at the South Pole. Flares with multiple times indicate an active period where X-ray emission rose and fell repeatedly within a short time frame but the X-ray emission is integrated over those sub-flares. This list of flares was extracted from the RHESSI catalog [5].



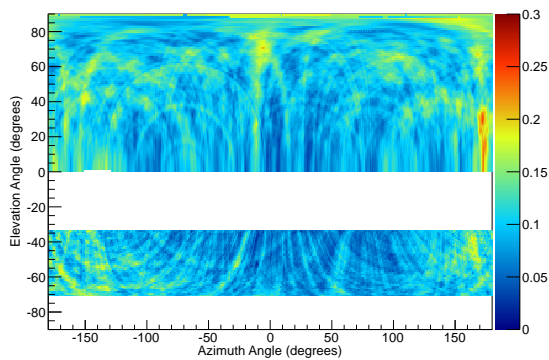
(a) Full waveform map



(b) "Before" map



(c) "During" map



(d) "After" map

Figure 19: The reconstruction maps for the event shown in Fig. 18 using (a) the full waveform, (b) only the "before" section of the waveform, (c) only the "during" section, and (d) only the "after" section.

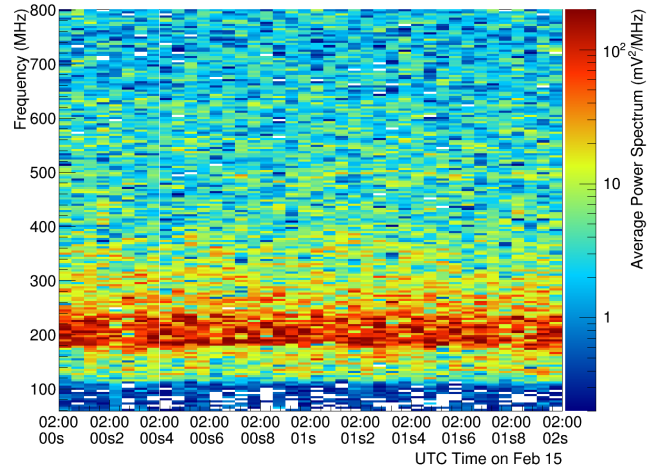
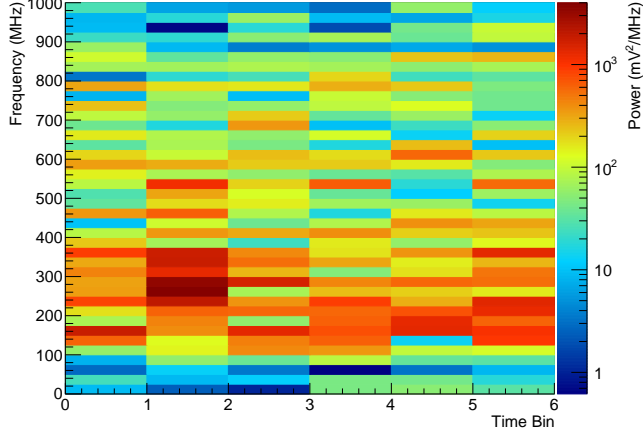


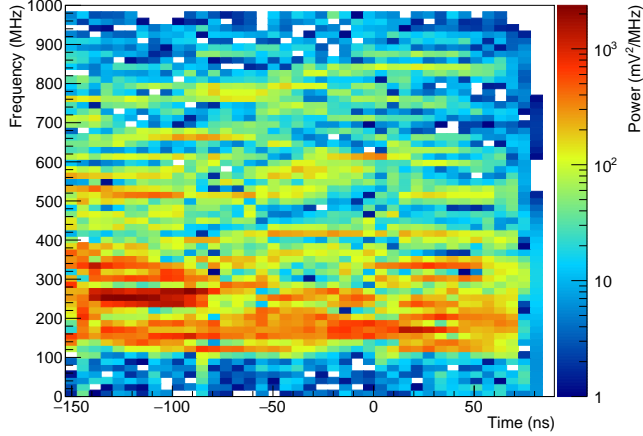
Figure 20: A spectrogram produced over a two second-long scale using 48 sequential events during the flare period. The events were recorded as RF triggers between 2:00:00 and 2:00:02 on Feb. 15th, 2011.

frequencies below about 150 MHz, and the ARA Testbed search for diffuse neutrinos rejected events with more than 10% of the power accounted for below 150 MHz. This cut was made to reduce anthropogenic background noise. In addition, the Feb. 13th flare did not produce any events that survived the "Reconstruction Quality Cut" imposed in the neutrino search, which required that the region in the sky that gives a high cross-correlation be narrow and unique. Fig. 22 shows a typical event during the time of the Feb. 13th flare. This map shows a broader range of directions that give cross-correlation values similar to the peak value, compared to the narrow peak typical of an event from the Feb. 15th flare. Additionally, the results shown in the previously published work on the Feb. 13th flare [3] only used the surface antennas which operate in a lower frequency band (30-300 MHz) than the borehole antennas used in this work (150-850 MHz).

The solar flare events from Feb. 13th failed to pass the "Reconstruction Quality Cut," which requires that the reconstruction map of a "well-reconstructed" event be both well-defined and unique. The key parameter of the cut is the area of the 85% contour around the absolute peak of the map. The conditions of the cut are two-fold. First, this area must be less than 50 square degrees in magnitude. This indicates that the reconstruction is "well-defined," and does not allow for a broad range of possible reconstruction locations within the peak contour. Second, the area around this peak must be no less than two-thirds of the total area on the map with a value of 85% of the peak or greater. This condition forces the event to be "unique," in that no other location on the sky reconstructs as well. A fuller description of the requirement can be found in [4].



(a) Spectrogram with independent time bins



(b) Spectrogram from running sub-samples of the waveform

Figure 21: Spectrogram created from a single waveform, measured in Channel 2, from the same event as shown in Figs. 8, 10 and 4. Figure (a) shows the spectrogram from 6 independent sub-samples of the waveform. Figure (b) shows the spectrogram taken from a running sub-window of the waveform. Although each sample is correlated with its neighbors in time, this approach yields finer frequency resolution due to the greater number of samples allowed.

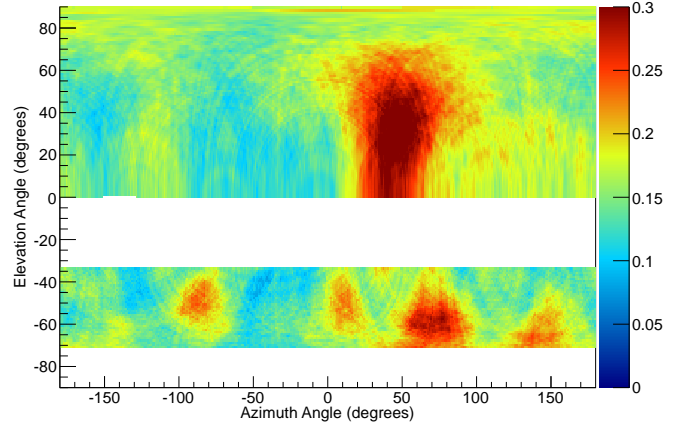


Figure 22: Reconstruction map for a typical event during the time of the Feb. 13th flare. This map shows a broader range of directions that give cross-correlation values similar to the peak value, compared to the narrow peak typical of an event from the Feb. 15th flare.